Stable and Highly Active Single Atom Configurations for Photocatalytic H_2 Generation

*Yue Wang, Nikita Denisov, Shanshan Qin, Danielle Santos Gonçalves, Hyesung Kim, Bidyut Bikash Sarma, and Patrik Schmuki**

The employment of single atoms (SAs), especially Pt SAs, as co-catalysts in photocatalytic H_2 generation has gained significant attention due to their exceptional efficiency. However, a major challenge in their application is the light-induced agglomeration of these SAs into less active nanosized particles under photocatalytic conditions. This study addresses the stability and reactivity of Pt SAs on TiO_2 surfaces by investigating various post-deposition annealing treatments in air, Ar, and Ar-H_2 environments at different temperatures. It is described that annealing in an Ar-H_2 atmosphere optimally stabilizes SA configurations, forming stable 2D rafts of assembled SAs ≈0.5–1 nm in diameter. These rafts not only resist light-induced agglomeration but also exhibit significantly enhanced H_2 production efficiency. The findings reveal a promising approach to maintaining the high reactivity of Pt SAs while overcoming the critical challenge of their stability under photocatalytic conditions.

1. Introduction

The exploration of supported single atoms (SAs) in catalysis has garnered significant attention across various disciplines, including heterogeneous catalysis,[1–5] electrocatalysis,[6–10] and most recently also in photocatalysis.[11–14] In classic photocatalytic reactions, a semiconductor is exposed to super-band-gap illumination, leading to the generation of mobile excited charge carriers (i.e., electrons and holes). These carriers have the capacity to migrate to the semiconductor surface, initiating reduction or oxidation reactions within the environment. A prominent focal point of investigation involves the transfer of photoexcited electrons from the semiconductor conduction band to water or H^+, culminating in the production of dihydrogen, H_2.[15,16] However, on numerous semiconductor surfaces, the progression of this step encounters kinetic impediments, necessitating catalysis typically facilitated by noble metals like Pt, Pd, Rh.[15,17] This phenomenon is also observed in the case of the most extensively researched photocatalyst, anatase TiO_2. The augmented catalytic activity conferred by these co-catalysts is commonly attributed to two principal factors: i) the formation of a Schottky-type contact with the semiconductor, thereby facilitating electron transfer through the attached noble metal, and ii) the promotion of a facilitated recombination reaction of H^0 species to H_2 ($2H^0 \rightarrow H_2$), particularly pronounced with Pt, Pd, Rh.[18–21] In conventional methodologies, co-catalysts are deposited in the form of nanoparticles (NPs), characterized by crystallites of a few nanometers in diameter, onto the semiconductor surface. To address economic considerations associated with noble metals and concurrently maximize catalytic activity, extensive efforts are directed toward optimizing particle loading and size.[22–28] Evidently, the utilization of single atoms represents a paradigm shift, affording a maximized surface-to-volume ratio for co-catalytic sites and, consequently, heightened reactivity, contingent upon adherence to downscaling laws.[29–31]

It is important to note that in contrast to classic catalysis, in photocatalysis, under common illumination conditions, not a maximum density of most active SA configurations (active sites) is desired, but an optimized interaction of the SA co-catalyst with the light and charge harvesting features of the underlying semiconductor. In many cases—such as for compact TiO_2 layers—a loading density of $\approx 10^5$ atoms μm^{-2} is sufficient[32] to reach a maximized co-catalytic effect.

Nevertheless, a considerable body of literature discusses the most active configuration of SAs on a substrate—not only in view

---

Y. Wang, N. Denisov, S. Qin, H. Kim, P. Schmuki
Department of Materials Science and Engineering
Chair for Surface Science and Corrosion (WW4-LKO)
Friedrich-Alexander-Universität Erlangen-Nürnberg
Martensstraße 7, 91058 Erlangen, Germany
E-mail: schmuki@ww.uni-erlangen.de

D. S. Gonçalves
Institute of Catalysis Research and Technology
Karlsruhe Institute of Technology
76344 Eggenstein-Leopoldshafen, Germany

B. B. Sarma
Institute of Catalysis Research and Technology and Institute for Chemical Technology and Polymer Chemistry
Karlsruhe Institute of Technology
76131 Karlsruhe, Germany

P. Schmuki
Regional Centre of Advanced Technologies and Materials
Šlechtitelů 27, Olomouc 78371, Czech Republic

The ORCID identification number(s) for the author(s) of this article can be found under https://doi.org/10.1002/adma.202400626

DOI: 10.1002/adma.202400626

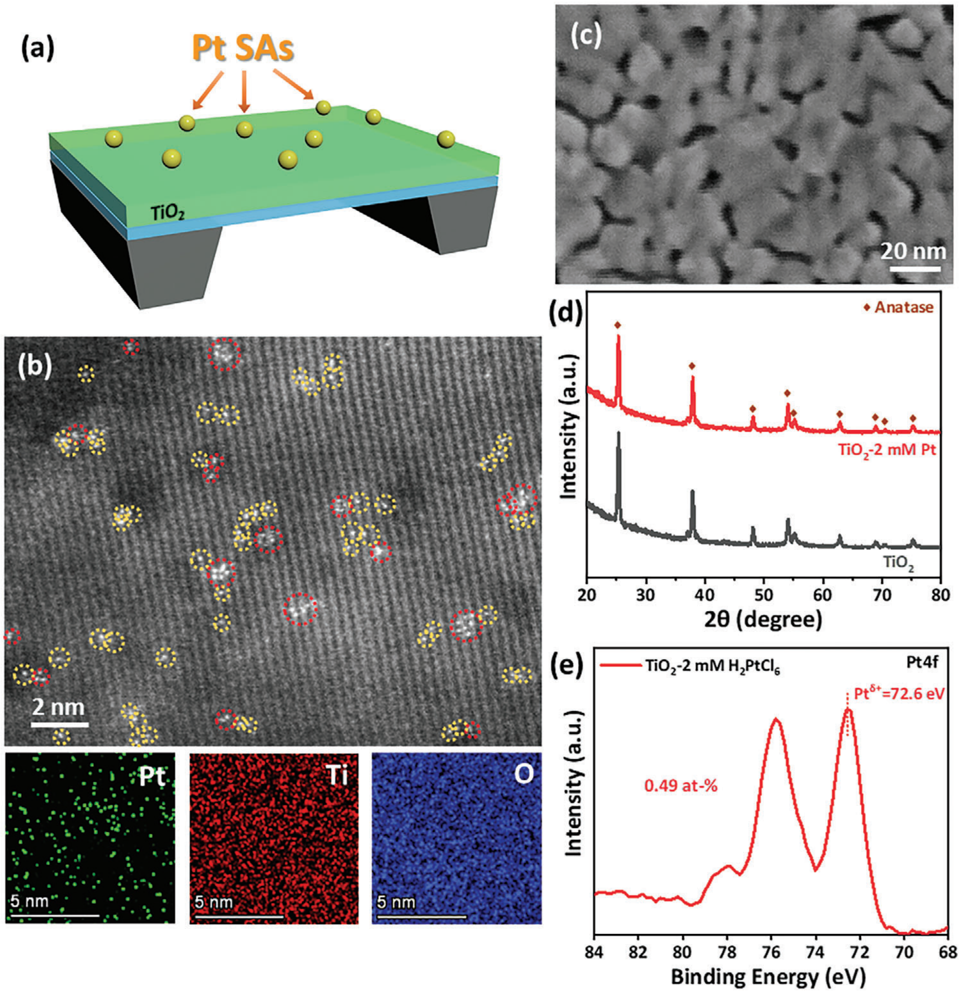

Figure 1. a) Schematic of a sputtered TiO_2 layer on TEM grid. b) HAADF-STEM image with energy-dispersive X-ray (EDX) mapping for different elements on the TiO_2 anatase layer after reactive deposition from 2 mM H_2PtCl_6. c) SEM image, d) XRD patterns, and e) XPS Pt4f spectrum of TiO_2 anatase layer after reactive deposition from 2 mM H_2PtCl_6.

of its detailed placement on/in a lattice but also in view of multi-atom configurations (e.g., dimers, trimers, few atom 2D rafts, etc.), which can strongly affect the metal-support and metal–hydrogen interactions. Interestingly, smaller-sized Pt clusters are often regarded as inferior for H_2 evolution, when compared to larger (≈1–3 nm) Pt NPs.[24,26,28,33–35] In addition, certain geometric features of the metal co-catalyst (e.g., facets, ridges, or corners) have been recognized as favorable for H-binding or H–H coupling.[23,25,33] While the debate on the ideal co-catalyst size for H_2 evolution is still ongoing, SAs have come out on top in many studies.[34–41]

In any case, a key issue in terms of exploiting SAs or few-atom clusters is the stabilization of the active site on the surface.[42,43] Agglomeration of SAs can be caused by thermally induced surface diffusion or, even more importantly in the case of photocatalysts, by light induced activation and agglomeration. Light-induced activation can within second-to-minute time scales lead to substantial agglomeration of SAs to nanosize metallic particles.[26,34,44]

For TiO_2, the benchmark semiconductor for photocatalytic H_2 generation, various strategies have been developed for the synthesis and dispersion of SA co-catalysts onto different titania geometries. These approaches typically involve impregnation methods based on strong electrostatic adsorption (SEA)[45–47] or reactive deposition.[39,48,49]

Common approaches for stabilization can exploit defect sites such as surface dislocations, oxo groups and vacancies to anchor the SAs.[50] In many approaches for catalyst preparation, after Pt precursor adsorption or reaction, an additional thermal treatment or thermal reduction step is applied, either to fully remove coordinated ligands from surface adsorbed precursor species, and/or to trigger anchoring by surface reactions.[26,41,44,51–53]

In the present work, we thus investigate the effect of post-deposition annealing in air, Ar, and Ar-H_2 on the configuration, stability, and reactivity of the Pt SAs as co-catalysts for photocatalytic H_2 generation.

In many previous works,[36,39,48–50,54–59] SA deposition was carried out on TiO_2 nanostructures (e.g., tubes,[54,55,57] flakes,[48,49] and powders[50,58,59]) in order to exploit the large surface area of the substrate for maximizing the overall performance.[55,59,60] In contrast, for our studies, we use direct current (DC) sputter deposited anatase thin films as the semiconductive platform for photocatalytic H_2 evolution. These compact, flat layers provide a simple and defined geometry for illumination and characterization, in terms of loading and distribution of SAs, as well as a most direct geometry for reactivity assessment.

After SA deposition, we investigate different post-deposition annealing treatments, namely in air, Ar and Ar-H_2 environments at temperatures ranging from 350 to 750 °C. We find that air and Ar annealing lead to nanoscale 3D agglomerates (nanoparticles) whereas in Ar-H_2 only very mild agglomeration to 2D rafts of ≈0.5–1 nm diameter takes place. Most importantly, this configuration shows not only the highest H_2 production activity but also an exceptional stability against the most critical form of co-catalyst activity loss: light induced agglomeration.

2. Results and Discussion

Defined compact anatase thin film substrates were produced by DC sputter deposition on SiO_2 substrates as described previously[61] and in the Experimental Section. For photocatalytic H_2 evolution measurements, we use these layers with a thickness of 200 nm (see Figure S1, Supporting Information). All samples after sputter deposition were annealed in air at 450 °C to form a defined anatase layer.[61] Pt SAs were deposited using a reactive deposition approach that relies on the reaction of titania defects when immersed in H_2PtCl_6 solution.[62] For transmission electron microscopy (TEM) investigations, 50 nm thick anatase films were fabricated under the same DC sputter deposition conditions on photolithographically defined TEM supports as schematically illustrated in **Figure 1**a, and as described in the Experimental Section and in previous work.[39]

These layers allow to obtain high-angle annular dark-field scanning transmission electron microscopy (HAADF-STEM) images of the anatase surfaces and atomic resolution for deposited Pt single atoms. Figure 1b shows HAADF-STEM image for such an anatase layer after Pt SAs were deposited from a 2 mM H_2PtCl_6 solution, and it clearly shows the presence of SAs dispersed on a lattice with a spacing of 0.35 nm that corresponds to the (101) planes of anatase. STEM elemental mapping (Figure 1b, lower part) further confirms the uniform distribution of Pt and the absence of crystallized Pt agglomerates on the surface. While SAs are present on the entire surface, also some mild agglomeration of SAs into 2D clusters becomes apparent (some examples are marked with red circles in Figure 1b). The estimated surface density of SAs ($\approx 1.7 \times 10^5\ \mu m^{-2}$) and clusters ($\approx 5.3 \times 10^4\ \mu m^{-2}$) is comparable to the "optimum" density described in previous work[32]—i.e., a density that is able to provide a sufficient (saturated) co-catalytic effect for these type of titania layers. For such SA decorated layers, as expected, high-resolution scanning electron microscope (SEM) does not show any visible Pt-deposits (Figure 1c) and X-ray diffraction (XRD) shows only peaks of anatase ($2\theta = 25.4°, 37.9°, 48.2°, 54.1°, 55.2°, 62.8°, 68.9°, 70.4°, 75.2°$), i.e., the XRD remains the same as before the Pt deposition (Figure 1d)—Pt cannot be detected.

However, a quantitative assessment of the Pt loading can be obtained from X-ray photoelectron spectroscopy (XPS). Figure 1e provides XPS high-resolution spectrum of the Pt4f region for loading from a 2 mM Pt-precursor solution—a total Pt surface concentration of 0.49 at% is obtained. In this work, we also used experiments at a lower precursor concentration (0.01 mM) which leads to a loading of 0.42 at% (see Figure S2, Supporting Information). In either case, the corresponding peak fittings for the Pt4$f_{7/2}$ peak yield a binding energy of 72.6 eV—this position corresponds to $Pt^{\delta+}$ with a nominal charge of $\delta \approx 2$, consistent with our previous works.[39,56,58]. That is, in the Pt attachment process, the Pt(IV) precursor reacts to a surface coordinated $Pt^{\delta+}$ state.

These SA decorated anatase layers were then tested for photocatalytic H_2 production from a methanol/water solution. In this widely used system, both H^+ reduction and methanol photoreforming reactions can yield H_2[63,64] with an estimated relative contribution of ≈1:2. **Figure 2**a shows the amount of photocatalytically produced H_2 under a 365 nm LED (65 mW cm^{-2}) illumination. Evidently, the deposition process leads directly to a highly active photocatalytic system.

Nevertheless, as discussed in previous work in detail,[34] illumination leads to a significant agglomeration of Pt SAs to 3D nanoparticles with crystallite sizes of 3–4 nm and these are easily detectable with SEM (Figure 2b) and TEM (Figure 2d). In XPS, Figure 2c, after illumination, the Pt4f is shifted to a binding energy of 70.8 eV which corresponds to metallic Pt.[34] Evidently, a vast amount of Pt SAs—under illumination—have agglomerated to metallic nanoparticles. This instability of SAs in photocatalysis is of a main concern for its long-term activity.

In a next step, we used thermal treatments of SA decorated surfaces in inert, oxidative, and reductive atmospheres and investigated the effects on reactivity and stability of the SA decorated surfaces.

Figure 3 shows the H_2 evolution performance for the layers (prepared as in Figure 1) after annealing in air (Figure 3a), Ar (Figure 3b), and Ar-H_2 (Figure 3c) at different temperatures. From the slopes of the curves, we can obtain the H_2 production rates of all the conditions in Figure 3d. Evidently, the heat treatment can strongly affect the efficiency of the annealed photocatalyst for H_2 production. While treatments in air in general provide a similar activity with the untreated SA decorated surface, especially treatments in Ar-H_2 can lead to a higher activity, and a peak efficiency is reached for treatments in Ar-H_2 at 450 °C.

In **Figure 4**, typical SEM images are compiled for the anatase surfaces after annealing in different atmospheres at 450 °C before (a) and after (b) illumination—the complete data (for all annealing conditions) are shown in Figures S3 and S4 (Supporting Information). From the SEM images in Figure 4a and Figure S3 (Supporting Information), it is evident that in general annealing in air leads to a strong agglomeration of the Pt SAs to nanoparticles—the higher the annealing temperature, the higher the particle diameter, for 350, 450, 750 °C, 3D-particles of ≈1–2, ≈2, and ≈30 nm can be found. For Ar, agglomeration is less pronounced and leads to 3D-particle sizes for 450 °C of ≈1–2 nm and increases only very little for 750 °C to ≈2–3 nm. These nanoparticles are well distributed over the surface, That is, Ar annealing also leads to agglomeration to nanoparticles but it leads to a well-defined NP decoration. Most importantly, in contrast to air or Ar, for annealing in Ar-H_2 no agglomeration can be observed in SEM in the range of annealing temperatures of 350 to 550 °C. Notably, the observed increase in the Pt agglomerates size and density

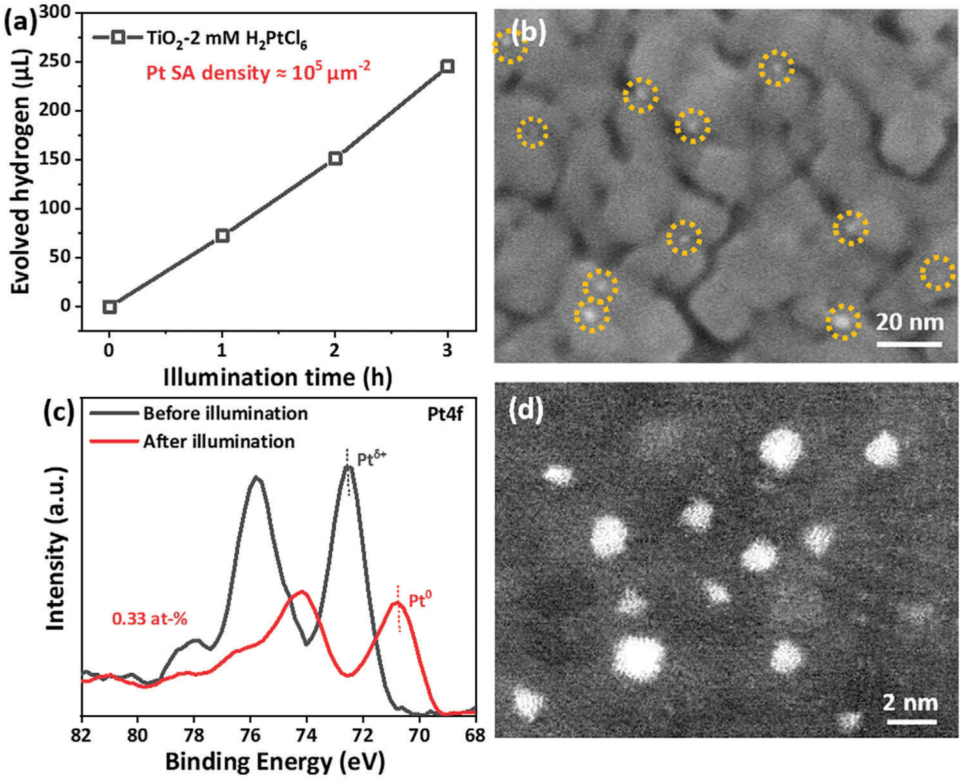

Figure 2. a) Photocatalytic H_2 evolution of TiO_2 anatase layers after reactive deposition from 2 mM H_2PtCl_6 and 3 h illumination. b) SEM image c) XPS Pt4f spectra and d) HAADF-TEM image of TiO_2 anatase layers after reactive deposition from 2 mM H_2PtCl_6 and 3 h illumination.

following the annealing clearly correlates with the degradation in performance (Figure 3d).

The observed effects of the annealing atmosphere on the Pt SA thermal stability and cluster size indicate that Pt interaction with the TiO_2 surface is significantly altered under oxidizing, inert, or reductive conditions. These atmosphere-induced effects can be divided into two categories: gas interaction effects and mobilizing Pt (as reported for Pt–H[34] or Pt–O[65–67] interactions), and annealing-induced changes of the TiO_2 support. The latter involves intrinsic defects of TiO_2 (e.g., oxygen vacancies and Ti^{3+}), which are expected to form under a reducing Ar-H_2 atmosphere in the studied temperature range. Such defective TiO_2 modifications have been previously used for stabilizing SAs,[38,41,68–70] and even for redispersing aggregated NPs.[37] Some theoretical studies further indicate that Pt SAs adsorbed on O-vacancy sites (i.e., via Ti-Pt-Ti surface coordination) possess the highest binding energy to the TiO_2 support.[70–73] Alternatively, Pt-O-Ti^{3+} coordination has been proposed as the most active for H_2 evolution.[38] In comparison to Ar-H_2, Ar atmosphere provides less reductive conditions, and accordingly it appears to be less effective in stabilizing SA anchoring.

Figure 4c (left) provides a compilation of the Pt4f$_{7/2}$ position (extracted from the XPS high-resolution spectra of the Pt4f region in Figure S5, Supporting Information) for the different treatments. At lower temperatures (350 °C) the Pt oxidation state is almost unaffected in air (Pt4f$_{7/2}$ $\approx$ 72.5 eV), while Ar and Ar-H_2 show a slight reducing effect (Pt4f$_{7/2}$ $\approx$ 71.8 eV). At higher temperatures in Ar ($\geq$450 °C) and air ($\geq$550 °C) the peak is shifted clearly to the metallic position of 70.4–70.9 eV with no trace of Pt-oxide formation in air (Figure S6, Supporting Information). This is well in line with the observations from SEM, i.e., the formation of 3D Pt NPs (Figure S3, Supporting Information).

In contrast to oxidizing (air) or inert (Ar) conditions, annealing in a reductive Ar-H_2 atmosphere leads to a different outcome. In this case, over a large range of annealing temperatures, the Pt4f$_{7/2}$ peak position remains above 71.4 eV. This indicates that the Pt signal originates predominantly from mildly oxidized Pt species (e.g., Pt SAs coordinated with terminal O-groups of TiO_2 and other Pt atoms). Additionally, the Pt4f$_{7/2}$ peak broadening indicates that a considerable fraction of SAs is aggregated and the formation of Pt-Pt bonds has taken place.

Notably, an apparent decrease of the Pt surface content with temperature (Figure 4c, right) also indicates an increase of the Pt agglomerate size (in line with Figure S3, Supporting Information). Specifically, the Pt4f signal attenuation in Pt agglomerates (with an estimated inelastic mean free path of ≈1.6 nm[74]) leads to underestimation of the Pt content by XPS.

In order to further characterize the nature of the Pt sites formed by different treatments, we studied CO adsorption at these sites by diffuse reflectance infrared Fourier transform spectroscopy (DRIFTS, **Figure** 5a–d) under a continuous flow of 1% CO/He gas mixture at room temperature. To provide a sufficient surface area required for CO adsorption studies, anatase powders were utilized as a support instead of layers and successfully loaded with Pt SAs (see Experimental Section for details), as

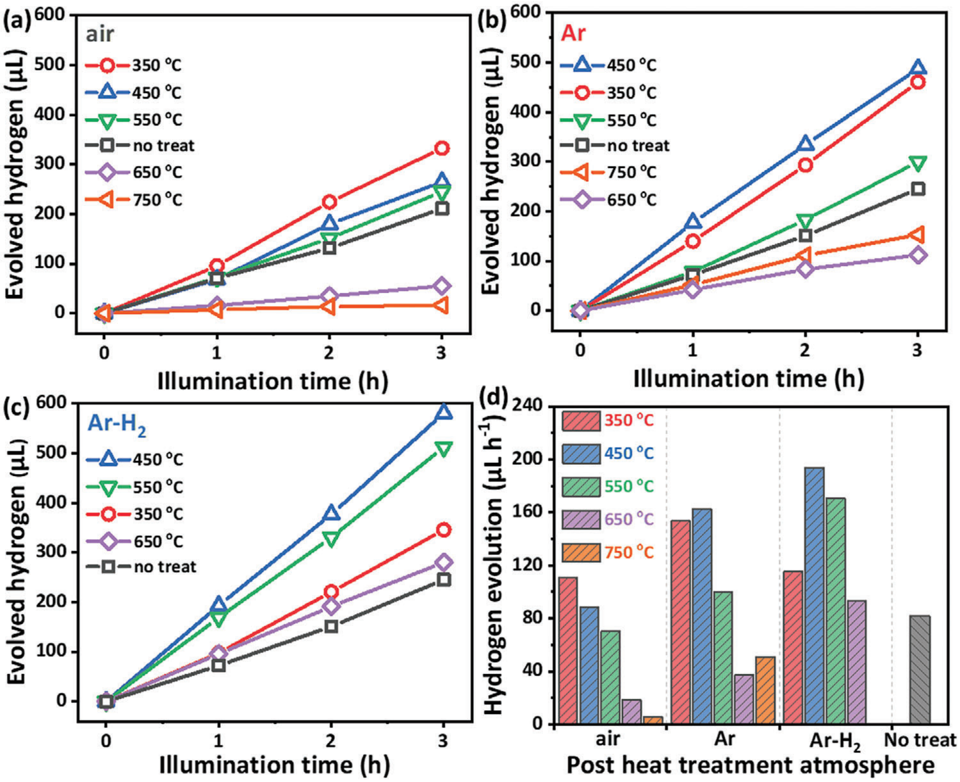

Figure 3. a–c) Photocatalytic H_2 evolution and d) normalized evolution rate of TiO_2 anatase layers after reactive deposition from 2 mM H_2PtCl_6, treated in various annealing conditions and illuminated for 3 h.

confirmed by XPS (Figure S7, Supporting Information). For the non-annealed SA decorated sample, we observed CO vibrational peak at 2102 cm^{-1}, which is characteristic of linearly bonded CO over Pt single site (usually Pt^{2+}).[52,75–77] Additional peak observed at 2172 cm^{-1} corresponds to gas phase CO.[76] Accordingly, upon switching from CO/He to pure He flow the peak at 2102 cm^{-1} is still present even after 1 h, while the peak at 2172 cm^{-1} instantly vanishes.

Consequent annealing of this sample at 450 °C leads to noticeable changes in the CO adsorption at Pt sites, depending on the atmosphere. For the sample annealed in air, two vibrational peaks were observed at 2092 and 2052 cm^{-1}, which correspond to CO adsorbed over partially reduced Pt SAs and Pt clusters, respectively.[51] For the Ar-annealed sample, a broad signal at 2060 cm^{-1} with a notable shoulder at 2075 cm^{-1} can be identified, which corresponds to CO adsorption over Pt clusters.[51] However, when the annealing atmosphere is changed from Ar to Ar/H_2 mixture, the CO vibrational peaks exhibit a shift to higher wavenumbers (2062 and 2084 cm^{-1}), indicating a different state of Pt species formed in presence of H_2. Notably, an elevated background signal (i.e., broad-band infrared signal) in DRIFTS spectra could result from the reduction of the TiO_2 support,[78–81] as it is observed only for the sample annealed in Ar-H_2 (Figure 5d), further suggesting a unique type of electronic metal–support interaction in this material. These findings are in line with the SEM and XPS investigations that reveal SA agglomeration to 3D nanoparticles in air and Ar, but different mild agglomeration features for Ar-H_2.

To further elucidate the effect of Ar-H_2 treatment, we carried out HAADF-STEM studies after Ar-H_2 annealing at 450 °C (**Figure 6**). Apparently, this heat treatment only introduces some very mild agglomeration of Pt SAs to 2D islands (rafts) of ≈0.5–1 nm in diameter that consist of 10–30 atoms. The fact that these clusters maintain a 2D structure clearly indicates a strong interaction of the aggregated Pt atoms with the TiO_2 surface, and also explains a partially reduced state of Pt found by XPS.

If we compare these results of the surface morphology with the data from XPS, we see that obviously thermal aggregation is strongly dependent on the atmosphere, as may be expected. In general, Pt SAs aggregation can be viewed as a thermally activated process of overcoming surface diffusion barriers, especially when an inert (Ar) atmosphere is used. As a result, Pt SAs generally tend to agglomerate during such heat treatments[44,51,52,60,82–84] and only very few studies have managed to successfully or partially stabilize Pt SAs on a TiO_2 surface even under relatively mild conditions (up to 400 °C).[38,41,51–53] At temperatures above 400 °C, the existence of isolated Pt SAs has not been reported.[37] However, our results show that even a pristine TiO_2 surface can provide a remarkable thermal stability for Pt SAs and the small (10–30 atoms) clusters under and after Ar-H_2 treatments.

However, in photocatalysis, thermal aggregation in the catalyst preparation step is only of minor concern. The much more severe issue is photoinduced agglomeration during illumination, as we pointed out in Figure 2 for the non-annealed Pt SA decorated TiO_2 surface.

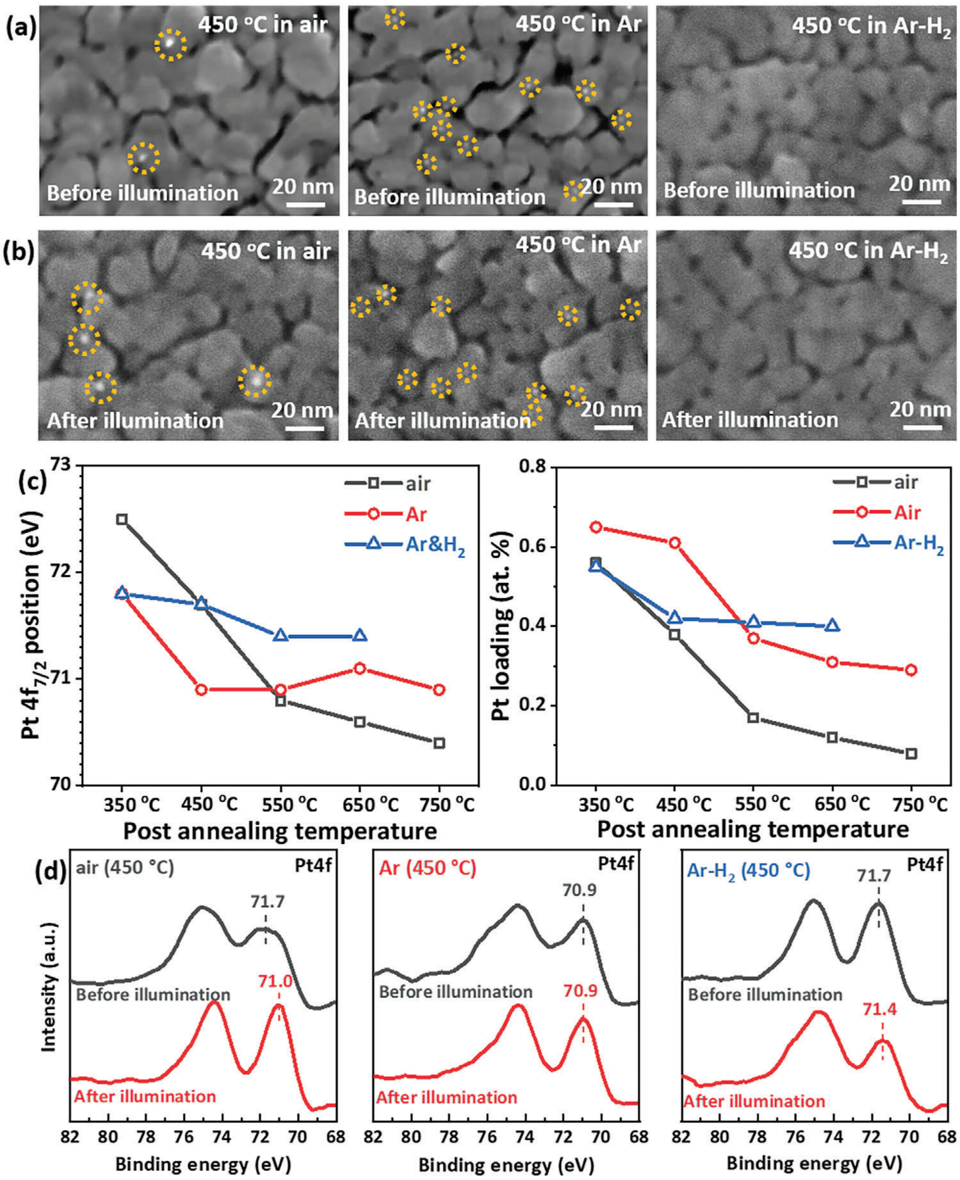

Figure 4. SEM images of TiO_2 anatase layers after reactive deposition from 2 mM H_2PtCl_6, a) post-annealed at 450 °C for 1 h in different atmospheres, and b) illuminated for 3 h. c) $Pt4f_{7/2}$ position and Pt loading of TiO_2 anatase layers after reactive deposition from 2 mM H_2PtCl_6 and treated in various annealing conditions. d) XPS Pt4f spectra of TiO_2 anatase layers after reactive deposition from 2 mM H_2PtCl_6 and post-annealed at 450 °C for 1 h in different atmospheres, then before and after 3 h illumination.

If we study the annealed surfaces after the photocatalytic experiments, we obtain the typical results shown in Figure 4b. In the case of Ar annealing, only mild changes in NP size or density can be seen—this implies that the thermally produced NPs also represent to some degree a stable form of Pt under photocatalytic conditions. In contrast, Ar-H_2 treated sample shows no signs of NPs neither after annealing nor even after illumination—a clear indication of the successfully stabilized Pt species in the form of 10–30 atoms, sub-nm scale rafts.

Figure 4d provides XPS high-resolution spectra of the Pt4f region for the different annealing environments (450 °C) after illumination. As expected, illumination has little effect on the Ar-annealed sample due to a near-complete thermal aggregation and reduction of Pt SAs to the metallic state ($Pt4f_{7/2}$ ≈ 70.9 eV). In contrast, air-annealed sample initially shows a broad $Pt4f_{7/2}$ signal (≈71.7 eV) from variously oxidized Pt species. However, such species are clearly unstable under illumination based on the $Pt4f_{7/2}$ peak shift toward a uniformly metallic state (≈71.0 eV). This is also in line with the observations from SEM where an increasing number of nm-size Pt crystals can be seen (Figure 4b).

For the Ar-H_2 annealed sample the situation is drastically different. The initial signal from oxidized Pt species (≈71.7 eV) shows a very small change even after illumination (≈71.4 eV).

HAADF-STEM for the Ar-H_2 annealed samples after illumination is shown in Figure 6b with highlighted Pt SAs. After illumination still the surface is covered exclusively with few-atom

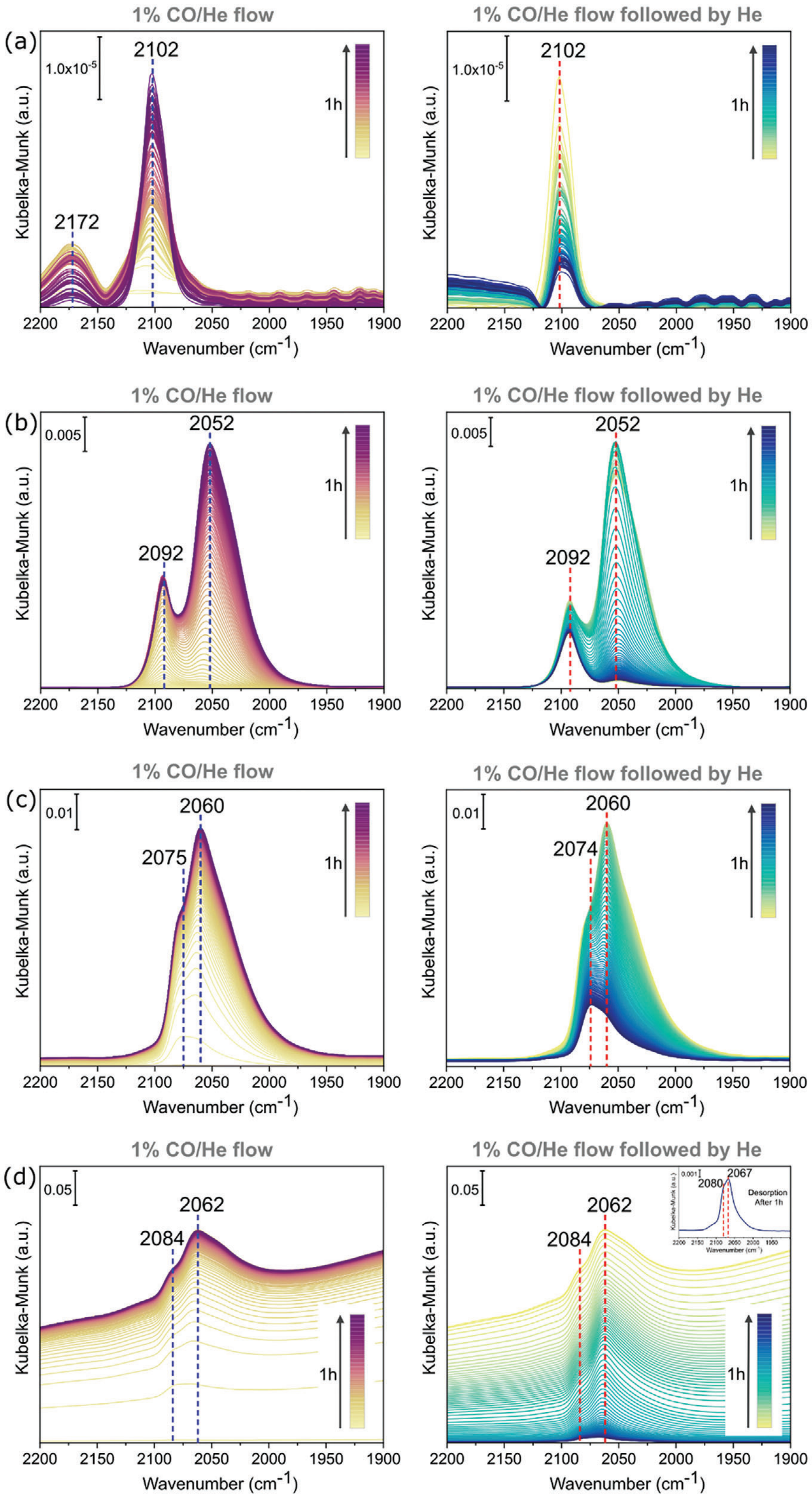

Figure 5. DRIFTS spectra of TiO_2 anatase layers a) after reactive deposition from 2 mM H_2PtCl_6, and post-annealed at 450 °C for 1 h in b) air, c) Ar, and d) Ar-H_2, respectively.

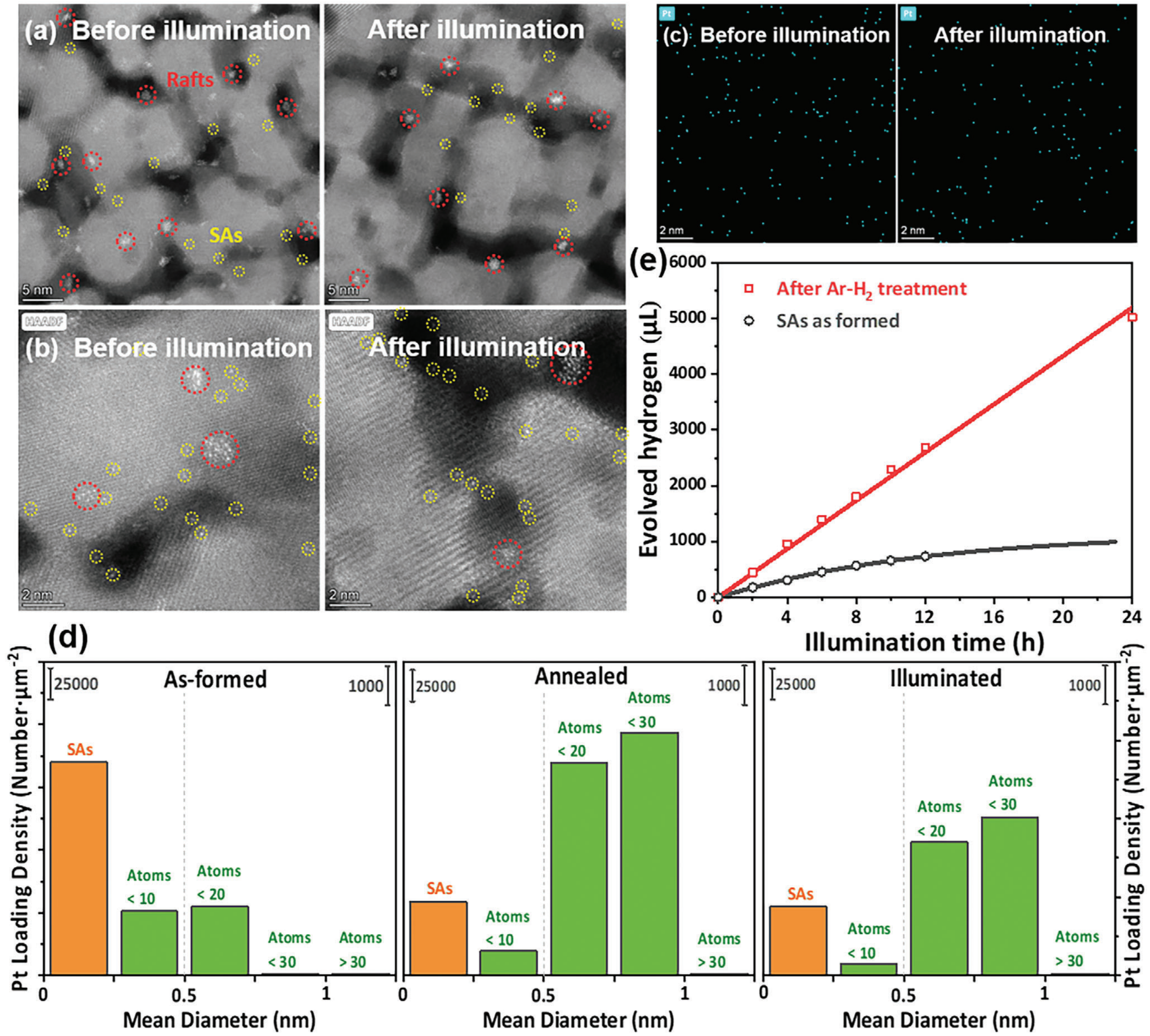

Figure 6. HAADF-STEM images with a) lower magnification, b) higher magnification, and c) energy-dispersive X-ray (EDX) mapping for Pt of TiO_2 anatase layers after reactive deposition from 2 mм H_2PtCl_6 and post-annealed at 450 °C for 1 h in Ar-H_2, then before and after 3 h illumination. d) Statistics of size distribution of SAs and agglomerates for TiO_2 anatase layers after reactive deposition from 2 mм H_2PtCl_6, post-annealed at 450 °C for 1 h in Ar-H_2 and illuminated for 3 h. e) Long-term photocatalytic H_2 evolution performance of Pt-SA-decorated TiO_2 anatase layers with and without treatment at 450 °C for 1 h in Ar-H_2.

2D rafts and SAs. The statistical distribution of Pt-SAs and assemblies for the as-deposited case, the Ar-H_2 annealed situation (450 °C) and the situation after annealing are compiled in Figure 6d—these data are obtained from an evaluation of several HAADF-STEM images. Evidently an Ar-H_2 treatment at 450 °C leads to some loss in SAs due to agglomeration into 2D rafts. The majority of the rafts formed are in the range of (10–30 atoms) with sizes in the range of 0.5–1 nm in diameter.

Combined with the SEM observations (Figure 4b), from Figure 6d it can be confirmed that for Ar-H_2 annealing only very minor changes (formation of rafts) occur during annealing and hardly any changes in the distribution of atomic features occur during light illumination. Also corresponding elemental mapping provided in Figure 6c shows a similar distribution of Pt on the surface before and after illumination.

The fact that the slightly agglomerated surface shows a higher H_2 evolution activity may suggest that minor agglomeration is beneficial to the overall activity but is—in any case—highly beneficial to the stability of the photocatalyst over extended illumination times.

To test for the stability of the beneficial effects on the long-term of the H_2 evolution induced by the Ar-H_2 annealing we carried out a photocatalytic experiment for extended times (Figure 6e) and compared it to a sample that was SA decorated by reactive deposition. Evidently, considerable activity decay is observed for the reference sample over time. In contrast, the Ar-H_2 annealed sample maintains its high activity without any notable change for over 24 h of illumination.

All in all, above results demonstrate that annealing in an Ar-H_2 atmosphere effectively prevents the agglomeration of Pt SA on TiO_2, leading to the formation of stable, two-dimensional configurations (Pt-raft assemblies) with diameters ranging from 0.5 to 1 nm. These configurations not only resist light-induced agglomeration but also show a remarkable increase in H_2 production efficiency.

3. Conclusions

In this study, we have conducted a comprehensive investigation into the use of platinum single atoms (Pt SAs) on TEM-transparent, flat anatase TiO_2 layers as co-catalysts for photocatalytic hydrogen (H_2) evolution. A notable challenge addressed is the propensity of these SAs to undergo "light-induced" agglomeration, leading to their transformation into less active nanoparticle forms under photocatalytic conditions. This phenomenon is a widespread issue in photocatalytic reactions.

Our work methodically examines a range of annealing treatments on SA-decorated surfaces. We demonstrate that specific annealing conditions not only further activate the photocatalysts but also significantly enhance the stability of the SA configurations on the TiO_2 surfaces. Particularly, annealing in an Ar-H_2 atmosphere facilitates the formation of minimally agglomerated, few-atom 2D rafts comprising 10–30 atoms. These configurations exhibit remarkable stability during thermal treatments and, crucially, show a substantial improvement in resistance to light-induced agglomeration.

The present work therefore mitigates a key destabilizing factor in the use of Pt SAs in photocatalysis while not compromising the very high reactivity of SAs (or few-atom assemblies).

4. Experimental Section

Materials: Methanol (99.9%, Carl Roth), ethanol ((99.8%, Carl Roth) and $H_2PtCl_6{\cdot}6H_2O$ (40.17% metallic Pt weight concentration, Metakem) were used without any additional purification. Silicon dioxide (SiO_2) coated silicon (Si) wafers (Si thickness = 380 μm ± 25 μm; SiO_2 coating thickness = 100 nm, MicroChemicals GmbH) were pretreated by O_2 plasma (SmartPlasma, Plasma technology GmbH). TEM supports (8 nm SiO_2 membrane with Si_3N_4 mesh on 200 μm silicon; Ted Pella, Inc. and PELCO International) were purchased from Plano GmbH. Anatase TiO_2 nanopowder (<25 nm particle size, 99.7%) was purchased from Sigma-Aldrich.

TiO_2 Layer Fabrication: TiO_2 layers were coated on flat SiO_2/Si wafer substrates by DC reactive magnetron sputtering (SP-P-US-6M-32 CreaTec Fischer & Co. GmbH), as previously demonstrated in literature.[61] Amorphous TiO_2 layers were sputtered in an Ar:O_2 atmosphere ($\approx 6.7 \times 10^{-3}$ mbar; volume ratio Ar:O_2 = 2:1) using a 5″ Ti target (99.995%, HMW Hauner GmbH & Co. KG) at 500 W for 4 h to reach the thickness of 200 nm. Afterward, the coated substrates were annealed in air (at 450 °C for 1 h).

For the transmission electron microscopy analysis, 50 nm thin TiO_2 layers were sputtered directly on TEM supports by the above-mentioned sputtering parameters with shorter deposition time (60 min), also followed by annealing at 450 °C for 1 h in air.

Pt Single Atom Deposition: Pt single atoms (SA) were loaded on the surface of TiO_2 anatase layers using an adopted "reactive deposition" approach[38,39,48,49,55,56,58] with $H_2PtCl_6{\cdot}6H_2O$ as the Pt source. 10 mL $H_2PtCl_6{\cdot}6H_2O$ aqueous solutions (0.01 or 2 mM) were prepared in quartz cells and purged with Ar gas to create anaerobic conditions. TiO_2 layers were immersed in the solutions afterward and kept in dark in sealed cells for 1 h. Finally, the samples were thoroughly cleaned with deionized water and dried with N_2 stream.

Similarly, Pt SA-loaded TiO_2 anatase powders were prepared. The powders (0.2 g L^{-1}) were dispersed in a quartz cell containing Ar purged $H_2PtCl_6{\cdot}6H_2O$ aqueous solution, and then the suspension was kept in dark with continuous stirring for 1 h. Upon completion, the powders were collected and washed three times by centrifuging and rinsing with DI water, then dried at 70 °C in air.

A series of Pt SA-loaded samples were subjected to further thermal treatments in air, Ar and Ar-H_2 environments at different temperatures for 1 h.

Characterization: High-angle annular dark-field scanning transmission electron microscopy (HAADF-STEM) images and EDX mapping of the samples were acquired by a probe-corrected scanning transmission electron microscope (Thermo Fisher Scientific Spectra 200). The surface and cross-section morphologies of the samples were investigated by field-emission scanning electron microscope (FE-SEM, S-4800, Hitachi). The crystalline structure of the samples was determined by X-ray diffraction (XRD, X'pert Philips MPD with a Panalytical X'celerator detector) by means of graphite monochromatized Cu Kα radiation (wavelength 1.5406 Å). The chemical composition of samples was analyzed by X-ray photoelectron spectroscopy (XPS, PHI 5600). All XPS spectra were shifted to a standard Ti2p binding energy in anatase of 458.5 eV and the peak deconvolution was carried out by MultiPak software.

Photocatalytic H_2 Evolution: Photocatalytic H_2 evolution performance of the Pt SA-loaded TiO_2 anatase layers was evaluated under UV illumination. The samples were placed in a quartz reactor containing 50 vol% methanol (hole scavenger) aqueous solution (10 mL), which was subsequently purged with Ar for 15 min. After that, the reactor was sealed, and illumination with an LED (λ = 365 nm, power density of 65 mW cm^{-2}, exposure area = 0.785 cm^2) was carried out for a specified duration. A gas chromatograph (GCMS-QO2010SE, SHIMADZU) equipped with a thermal conductivity detector (TCD) was used to determine the amount of H_2 generated at specific time intervals.

Diffuse Reflectance Infrared Fourier Transform Spectroscopy (DRIFTS): CO adsorption-DRIFTS investigations were carried out on a Tensor 27 FTIR spectrometer (Bruker) in a Harrick in situ diffuse reflectance cell covered with a CaF_2 window. Prior to measurements, the differently treated powdered samples were sieved to a size fraction of 100–200 μm. Then, the samples were purged with He via a mass flow controller and heated to 353 K to remove weakly bound impurities over a time period of 1 h. The spectra were collected in reflectance (R) mode under 1% CO/He gas flow at room temperature in the wavenumber range of 1000–4000 cm^{-1} with spectral resolution of 6 cm^{-1}.

The measurements were performed continuously with a duration of 1 h. 100 scans were collected for background spectra (under He flow) and 90 scans were collected for the measurement of each sample. The composition of the gas mixture was constantly monitored by a quadrupole mass spectrometer. The recorded spectra were reported in Kubelka–Munk (KM) units.

Supporting Information

Supporting Information is available from the Wiley Online Library or from the author.

Acknowledgements

Y.W. and N.D. contributed equally to this work. The authors would like to acknowledge the support from DFG and the European

Union's Horizon 2020 project SAN4Fuel (HORIZON-WIDERA-2021-ACCESS-03-01: 101079384). The authors also acknowledge the support from the Operational Program Research, Development and Education (European Regional Development Fund, Project No. CZ.02.1.01/0.0/0.0/15_003/0000416 of the Ministry of Education, Youth and Sports of the Czech Republic). PS particularly acknowledges the Czech Science Foundation project GA CR-EXPRO (23-08019X). The authors gratefully acknowledge the support of the Center for Nanoanalysis and Electron Microscopy (CENEM, Friedrich-Alexander-Universität Erlangen-Nürnberg).

Open access funding enabled and organized by Projekt DEAL.

Conflict of Interest

The authors declare no conflict of interest.

Data Availability Statement

The data that support the findings of this study are available from the corresponding author upon reasonable request.

Keywords

photocatalytic H_2 generation, Pt co-catalyst, single atom configurations, sputtered anatase layers

Received: January 12, 2024
Revised: March 5, 2024
Published online: April 4, 2024

---

[1] Y. Chen, S. Ji, C. Chen, Q. Peng, D. Wang, Y. Li, *Joule* **2018**, *2*, 1242.
[2] H. Zhang, G. Liu, L. Shi, J. Ye, *Adv. Energy Mater.* **2018**, *8*, 1701343.
[3] S. Mitchell, J. Pérez-Ramírez, *Nat. Commun.* **2020**, *11*, 4302.
[4] D. Liu, Q. He, S. Ding, L. Song, *Adv. Energy Mater.* **2020**, *10*, 2001482.
[5] X. Li, X. Yang, Y. Huang, T. Zhang, B. Liu, *Adv. Mater.* **2019**, *31*, 1902031.
[6] Y. Zhou, J. Li, X. Gao, W. Chu, G. Gao, L.-W. Wang, *J. Mater. Chem. A* **2021**, *9*, 9979.
[7] Q. Zhang, J. Guan, *Adv. Funct. Mater.* **2020**, *30*, 2000768.
[8] C. Zhu, S. Fu, Q. Shi, D. Du, Y. Lin, *Angew. Chem.* **2017**, *56*, 13944.
[9] J. Su, R. Ge, Y. Dong, F. Hao, L. Chen, *J. Mater. Chem. A* **2018**, *6*, 14025.
[10] W. Zang, Z. Kou, S. J. Pennycook, J. Wang, *Adv. Energy Mater.* **2020**, *10*, 1903181.
[11] Q. Zhang, J. Guan, *Sol. RRL* **2020**, *4*, 2000283.
[12] Q. Wang, D. Zhang, Y. Chen, W.-F. Fu, X.-J. Lv, *ACS Sustainable Chem. Eng.* **2019**, *7*, 6430.
[13] J. Fu, S. Wang, Z. Wang, K. Liu, H. Li, H. Liu, J. Hu, X. Xu, H. Li, M. Liu, *Front. Phys.* **2020**, *15*, 33201.
[14] F. Zhang, Y. Zhu, Q. Lin, L. Zhang, X. Zhang, H. Wang, *Energy Environ. Sci.* **2021**, *14*, 2954.
[15] X. Chen, S. Shen, L. Guo, S. S. Mao, *Chem. Rev.* **2010**, *110*, 6503.
[16] A. J. Bard, *J. Photochem.* **1979**, *10*, 59.
[17] S. Bai, W. Yin, L. Wang, Z. Li, Y. Xiong, *RSC Adv.* **2016**, *6*, 57446.
[18] K. G. Pickup, B. M. W. Trapnell, *J. Chem. Phys.* **1956**, *25*, 182.
[19] S. Katz, G. B. Kistiakowsky, R. F. Steiner, *J. Am. Chem. Soc.* **1949**, *71*, 2258.
[20] W. V. Smith, *J. Chem. Phys.* **1943**, *11*, 110.
[21] J. Schneider, M. Matsuoka, M. Takeuchi, J. Zhang, Y. Horiuchi, M. Anpo, D. W. Bahnemann, *Chem. Rev.* **2014**, *114*, 9919.
[22] C. Dong, C. Lian, S. Hu, Z. Deng, J. Gong, M. Li, H. Liu, M. Xing, J. Zhang, *Nat. Commun.* **2018**, *9*, 1252.
[23] J. Ma, X. Tan, Q. Zhang, Y. Wang, J. Zhang, L. Wang, *ACS Catal.* **2021**, *11*, 3352.
[24] Y. Ben-Shahar, F. Scotognella, I. Kriegel, L. Moretti, G. Cerullo, E. Rabani, U. Banin, *Nat. Commun.* **2016**, *7*, 10413.
[25] F. Xue, C. Chen, W. Fu, M. Liu, C. Liu, P. Guo, S. Shen, *J. Phys. Chem. C* **2018**, *122*, 25165.
[26] C. Dessal, L. Martínez, C. Maheu, T. Len, F. Morfin, J. L. Rousset, E. Puzenat, P. Afanasiev, M. Aouine, L. Soler, J. Llorca, L. Piccolo, *J. Catal.* **2019**, *375*, 155.
[27] D. Riassetto, C. Holtzinger, M. Langlet, *J. Mater. Sci.* **2009**, *44*, 2637.
[28] I. Vamvasakis, B. Liu, G. S. Armatas, *Adv. Funct. Mater.* **2016**, *26*, 8062.
[29] S. Gutić, A. Dobrota, E. Fako, N. Skorodumova, N. López, I. Pašti, *Catalysts* **2020**, *10*, 290.
[30] M. Li, K. Duanmu, C. Wan, T. Cheng, L. Zhang, S. Dai, W. Chen, Z. Zhao, P. Li, H. Fei, Y. Zhu, R. Yu, J. Luo, K. Zang, Z. Lin, M. Ding, J. Huang, H. Sun, J. Guo, X. Pan, W. A. Goddard, P. Sautet, Y. Huang, X. Duan, *Nat. Catal.* **2019**, *2*, 495.
[31] K. Maiti, S. Maiti, M. T. Curnan, H. J. Kim, J. W. Han, *Adv. Energy Mater.* **2021**, *11*, 2101670.
[32] S. Qin, J. Will, H. Kim, N. Denisov, S. Carl, E. Spiecker, P. Schmuki, *ACS Energy Lett.* **2023**, *8*, 1209.
[33] D. Wang, Z.-P. Liu, W.-M. Yang, *ACS Catal.* **2018**, *8*, 7270.
[34] N. Denisov, S. Qin, J. Will, B. N. Vasiljevic, N. V. Skorodumova, I. A. Pašti, B. B. Sarma, B. Osuagwu, T. Yokosawa, J. Voss, J. Wirth, E. Spiecker, P. Schmuki, *Adv. Mater.* **2023**, *35*, 2206569.
[35] J. Xing, H. B. Jiang, J. F. Chen, Y. H. Li, L. Wu, S. Yang, L. R. Zheng, H. F. Wang, P. Hu, H. J. Zhao, H. G. Yang, *J. Mater. Chem. A* **2013**, *1*, 15258.
[36] J. Xing, J. F. Chen, Y. H. Li, W. T. Yuan, Y. Zhou, L. R. Zheng, H. F. Wang, P. Hu, Y. Wang, H. J. Zhao, Y. Wang, H. G. Yang, *Chemistry* **2014**, *20*, 2138.
[37] J. Cai, A. Cao, Z. Wang, S. Lu, Z. Jiang, X.-Y. Dong, X. Li, S.-Q. Zang, *J. Mater. Chem. A* **2021**, *9*, 13890.
[38] Y. Chen, S. Ji, W. Sun, Y. Lei, Q. Wang, A. Li, W. Chen, G. Zhou, Z. Zhang, Y. Wang, L. Zheng, Q. Zhang, L. Gu, X. Han, D. Wang, Y. Li, *Angew. Chem.* **2020**, *132*, 1311.
[39] S. Hejazi, S. Mohajernia, B. Osuagwu, G. Zoppellaro, P. Andryskova, O. Tomanec, S. Kment, R. Zbořil, P. Schmuki, *Adv. Mater.* **2020**, *32*, 1908505.
[40] Q. Zuo, T. Liu, C. Chen, Y. Ji, X. Gong, Y. Mai, Y. Zhou, *Angew. Chem.* **2019**, *58*, 10198.
[41] X. Hu, J. Song, J. Luo, H. Zhang, Z. Sun, C. Li, S. Zheng, Q. Liu, *J. Energy Chem.* **2021**, *62*, 1.
[42] H. Hu, J. Wang, P. Tao, C. Song, W. Shang, T. Deng, J. Wu, *J. Mater. Chem. A* **2022**, *10*, 5835.
[43] Y. Chen, Z. Huang, Z. Ma, J. Chen, X. Tang, *Catal. Sci. Technol.* **2017**, *7*, 4250.
[44] L. Liu, D. M. Meira, R. Arenal, P. Concepcion, A. V. Puga, A. Corma, *ACS Catal.* **2019**, *9*, 10626.
[45] J. T. Miller, M. Schreier, A. J. Kropf, J. R. Regalbuto, *J. Catal.* **2004**, *225*, 203.
[46] J. Sun, J. Zhang, H. Fu, H. Wan, Y. Wan, X. Qu, Z. Xu, D. Yin, S. Zheng, *Appl. Catal., B* **2018**, *229*, 32.
[47] X. Chen, X.-B. Wang, S. Han, D. Wang, C. Li, W. Guan, W.-Y. Li, C. Liang, *ACS Appl. Mater. Interfaces* **2022**, *14*, 590.
[48] G. Cha, I. Hwang, S. Hejazi, A. S. Dobrota, I. A. Pašti, B. Osuagwu, H. Kim, J. Will, T. Yokosawa, Z. Badura, Š. Kment, S. Mohajernia, A. Mazare, N. V. Skorodumova, E. Spiecker, P. Schmuki, *iScience* **2021**, *24*, 102938.
[49] G. Cha, A. Mazare, I. Hwang, N. Denisov, J. Will, T. Yokosawa, Z. Badura, G. Zoppellaro, A. B. Tesler, E. Spiecker, P. Schmuki, *Electrochim. Acta* **2022**, *412*, 140129.

[50] S.-M. Wu, I. Hwang, B. Osuagwu, J. Will, Z. Wu, B. B. Sarma, F.-F. Pu, L.-Y. Wang, Z. Badura, G. Zoppellaro, E. Spiecker, P. Schmuki, *ACS Catal.* **2023**, *13*, 33.

[51] L. DeRita, S. Dai, K. Lopez-Zepeda, N. Pham, G. W. Graham, X. Pan, P. Christopher, *J. Am. Chem. Soc.* **2017**, *139*, 14150.

[52] H. V. Thang, G. Pacchioni, L. DeRita, P. Christopher, *J. Catal.* **2018**, *367*, 104.

[53] L. Chen, R. R. Unocic, A. S. Hoffman, J. Hong, A. H. Braga, Z. Bao, S. R. Bare, J. Szanyi, *JACS Au* **2021**, *1*, 977.

[54] X. Zhou, I. Hwang, O. Tomanec, D. Fehn, A. Mazare, R. Zboril, K. Meyer, P. Schmuki, *Adv. Funct. Mater.* **2021**, *31*, 2102843.

[55] Z. Wu, I. Hwang, G. Cha, S. Qin, O. Tomanec, Z. Badura, S. Kment, R. Zboril, P. Schmuki, *Small* **2022**, *18*, 2104892.

[56] Y. Wang, I. Hwang, Z. Wu, P. Schmuki, *Electrochem. Commun.* **2021**, *133*, 107166.

[57] I. Hwang, A. Mazare, J. Will, T. Yokosawa, E. Spiecker, P. Schmuki, *Adv. Funct. Mater.* **2022**, *32*, 2207849.

[58] S. Qin, N. Denisov, J. Will, J. Kolařík, E. Spiecker, P. Schmuki, *Sol. RRL* **2022**, *6*, 2101026.

[59] S. Qin, N. Denisov, B. B. Sarma, I. Hwang, D. E. Doronkin, O. Tomanec, S. Kment, P. Schmuki, *Adv. Mater. Interfaces* **2022**, *9*, 2200808.

[60] L. DeRita, J. Resasco, S. Dai, A. Boubnov, H. V. Thang, A. S. Hoffman, I. Ro, G. W. Graham, S. R. Bare, G. Pacchioni, X. Pan, P. Christopher, *Nat. Mater.* **2019**, *18*, 746.

[61] H. Kim, Y. Wang, N. Denisov, Z. Wu, Š. Kment, P. Schmuki, *J. Mater. Sci.* **2022**, *57*, 12960.

[62] Y. Wang, S. Qin, N. Denisov, H. Kim, Z. Bad’ura, B. B. Sarma, P. Schmuki, *Adv. Mater.* **2023**, *35*, 2211814.

[63] L. Chang, S.-T. Yong, S.-P. Chai, L. K. Putri, L.-L. Tan, A. R. Mohamed, *Mater. Today Chem.* **2023**, *27*, 101334.

[64] J. Zhao, R. Shi, Z. Li, C. Zhou, T. Zhang, *Nano Sel.* **2020**, *1*, 12.

[65] T. J. Lee, Y. G. Kim, *J. Catal.* **1984**, *90*, 279.

[66] X. Zhang, Z. Li, W. Pei, G. Li, W. Liu, P. Du, Z. Wang, Z. Qin, H. Qi, X. Liu, S. Zhou, J. Zhao, B. Yang, W. Shen, *ACS Catal.* **2022**, *12*, 3634.

[67] P. N. Plessow, F. Abild-Pedersen, *ACS Catal.* **2016**, *6*, 7098.

[68] Z. Tian, Y. Da, M. Wang, X. Dou, X. Cui, J. Chen, R. Jiang, S. Xi, B. Cui, Y. Luo, H. Yang, Y. Long, Y. Xiao, W. Chen, *Nat. Commun.* **2023**, *14*, 142.

[69] H. Pan, X. Wang, Z. Xiong, M. Sun, M. Murugananthan, Y. Zhang, *Environ. Res.* **2021**, *198*, 111176.

[70] S. Cai, L. Wang, S. Heng, H. Li, Y. Bai, D. Dang, Q. Wang, P. Zhang, C. He, *J. Phys. Chem. C* **2020**, *124*, 24566.

[71] T.-Y. Chang, Y. Tanaka, R. Ishikawa, K. Toyoura, K. Matsunaga, Y. Ikuhara, N. Shibata, *Nano Lett.* **2014**, *14*, 134.

[72] Y. Zhang, Y. Wang, K. Su, F. Wang, *J. Mol. Model.* **2022**, *28*, 175.

[73] J. Wan, W. Chen, C. Jia, L. Zheng, J. Dong, X. Zheng, Y. Wang, W. Yan, C. Chen, Q. Peng, D. Wang, Y. Li, *Adv. Mater.* **2018**, *30*, 1705369.

[74] C. J. Powell, A. Jablonski, NIST Electron Inelastic-Mean-Free-Path database - version 1.2 **2010**, https://www.nist.gov/srd/nist-standard-reference-database-71.

[75] K. Ding, A. Gulec, A. M. Johnson, N. M. Schweitzer, G. D. Stucky, L. D. Marks, P. C. Stair, *Science* **2015**, *350*, 189.

[76] L. Nie, D. Mei, H. Xiong, B. Peng, Z. Ren, X. I. P. Hernandez, A. DeLaRiva, M. Wang, M. H. Engelhard, L. Kovarik, A. K. Datye, Y. Wang, *Science* **2017**, *358*, 1419.

[77] Q. Liu, Z. Zhang, *Catal. Sci. Technol.* **2019**, *9*, 4821.

[78] C. D. Powell, A. W. Daigh, M. N. Pollock, B. D. Chandler, C. J. Pursell, *J. Phys. Chem. C* **2017**, *121*, 24541.

[79] A. Mahdavi-Shakib, K. B. S. Kumar, T. N. Whittaker, T. Xie, L. C. Grabow, R. M. Rioux, B. D. Chandler, *Angew. Chem.* **2021**, *133*, 7814.

[80] A. Walter, W. Eisenreich, G. Storch, *Angew. Chem.* **2023**, *62*, 202310634.

[81] X. Wang, A. Rosspeintner, A. Ziarati, J. Zhao, T. Bürgi, *Nat. Commun.* **2022**, *13*, 5458.

[82] A. Corma, P. Serna, P. Concepción, J. J. Calvino, *J. Am. Chem. Soc.* **2008**, *130*, 8748.

[83] C. Dessal, A. Sangnier, C. Chizallet, C. Dujardin, F. Morfin, J.-L. Rousset, M. Aouine, M. Bugnet, P. Afanasiev, L. Piccolo, *Nanoscale* **2019**, *11*, 6897.

[84] S. Duan, R. Wang, J. Liu, *Nanotechnology* **2018**, *29*, 204002.